A new model for global landslide susceptibility assessment and scenario-based hazard assessment

Rosa M. Palau[1], Farrokh Nadim[1], Eivind Paulsen[1], Erlend Storrøsten[1]

[1] Norwegian Geotechnical Institute, PO Box 3930 Ullevål Stadion, N-0806 Oslo, Norway.

Abstract

This paper presents the approach used to assess the global landslide hazard in the derivation of the Global Infrastructure Resilience Index (GIRI) for the Biennial Global Infrastructure Resilience Report of the Coalition for Disaster Resilient Infrastructure (CDRI). The methodology involves integrating landslide susceptibility and earthquake characteristics or rainfall data to determine, on a global scale, the probability of earthquake- and precipitation-induced landslides. The latter is assessed for both present and future climate conditions. The susceptibility map categorizes different terrains into five susceptibility classes, considering factors such as slope, vegetation (land use), lithology, and soil moisture, using global datasets. Rainfall information is gathered from the W5E5 dataset for the time span of 1979-2016 and the IPSL-CM6A-LR climate model from the ISIMIP3b dataset, covering the SSP126 and SSP585 scenarios for 2061-2100. To evaluate the potential for rainfall-triggered landslides, 24-hour rainfall intensities are utilized to classify areas into five rainfall hazard classes. The potential for earthquake-induced landslides is assessed based on the peak ground acceleration (PGA) of the earthquake event (scenario) at a given location and the susceptibility index of the terrain at that location. The landslide susceptibility map(s) and rainfall data or earthquake PGA are combined to produce a hazard matrix. The result is a probabilistic hazard map that can be used for scenario-based assessment of global landslide risk to critical infrastructure, with a resolution of three arc seconds (approximately 90 metres at the equator) for the whole globe.

Keywords: Landslides, rainfall-induced, earthquake-induced, climate change, hazard, global scale

1. Introduction

Rainfall- and earthquake-induced landslides represent an important hazard in mountainous regions worldwide. Landslides commonly impact the functioning of infrastructure assets such as roads and railways and occasionally damage buildings or result in fatalities (Petley 2012; Froude and Petley 2018). Precipitation-induced landslides are commonly triggered by rather short and intense rainfall events (Caine 1980; Guzzetti et al. 2008). As a consequence of climate change, the frequency and intensity of severe rainfall events that usually trigger landslides is expected to increase in some regions (Gariano and Guzzetti 2016). In addition, due to societal changes, tourism development, and the increased use of transport networks in mountain areas, the exposure of communities to landslides is growing in many parts of the world. Thus, understanding how the landslide hazard will change in

future is key to planning mitigation measures along linear infrastructure and reducing the risk to the population. Earthquakes are another common triggering mechanism of landslides (e.g. Keefer 1984). Landslides triggered by strong earthquakes in mountainous areas often have catastrophic consequences. For example, about 25% of the 87,000 casualties (69,000 confirmed killed and 18,000 missing) caused by Wenchuan Earthquake of 12 May 2008 were due to the landslides triggered by that event (Zhang et al. 2014).

Within the Natural Disaster Hotspots project (Dilley 2005; Nadim et al. 2006), landslide hazard maps were developed using global topography, lithology, earthquake and climate datasets to identify the most exposed countries. Subsequently, this approach was refined and improved and has been employed in various global (Nadim et al. 2013) and continental (Jaedicke et al. 2014) studies including the Global Assessment Reports (GAR) of UNDRR (then UNISDR).

The aim of this paper is to present the components of the landslide hazard model developed for the Flagship Report of The Coalition for Disaster Resilient Infrastructure (CDRI) to evaluate the global risk posed by earthquake- and rainfall-induced landslides to road and railway infrastructure, the latter both for the present climate regime and for future climate scenarios. The model presented in this paper (herein referred to as the GIRI landslide model) has a resolution that is about 10 times greater than the GAR model, and it can be used for the assessment of landslide probability for specific rainfall and earthquake scenarios.

2. The GIRI landslide model

The GIRI model is based on the model that was originally developed by (Nadim et al. 2006) in the project "Natural disaster hotspots – a global risk report" for the World Bank (Dilley 2005) to identify the global landslide hazard and risk "hotspots". Its inputs are (i) susceptibility information, and (ii) gridded information of different scenarios for each of the landslide-triggering factors, including rainfall and earthquake. The output consists of global scenario-based landslide hazard maps that can be used to evaluate the risk to linear infrastructure. Figure 1 shows a general flowchart of the GIRI landslide model.

In the following sections, the components of the GIRI landslide model are explained in more detail.

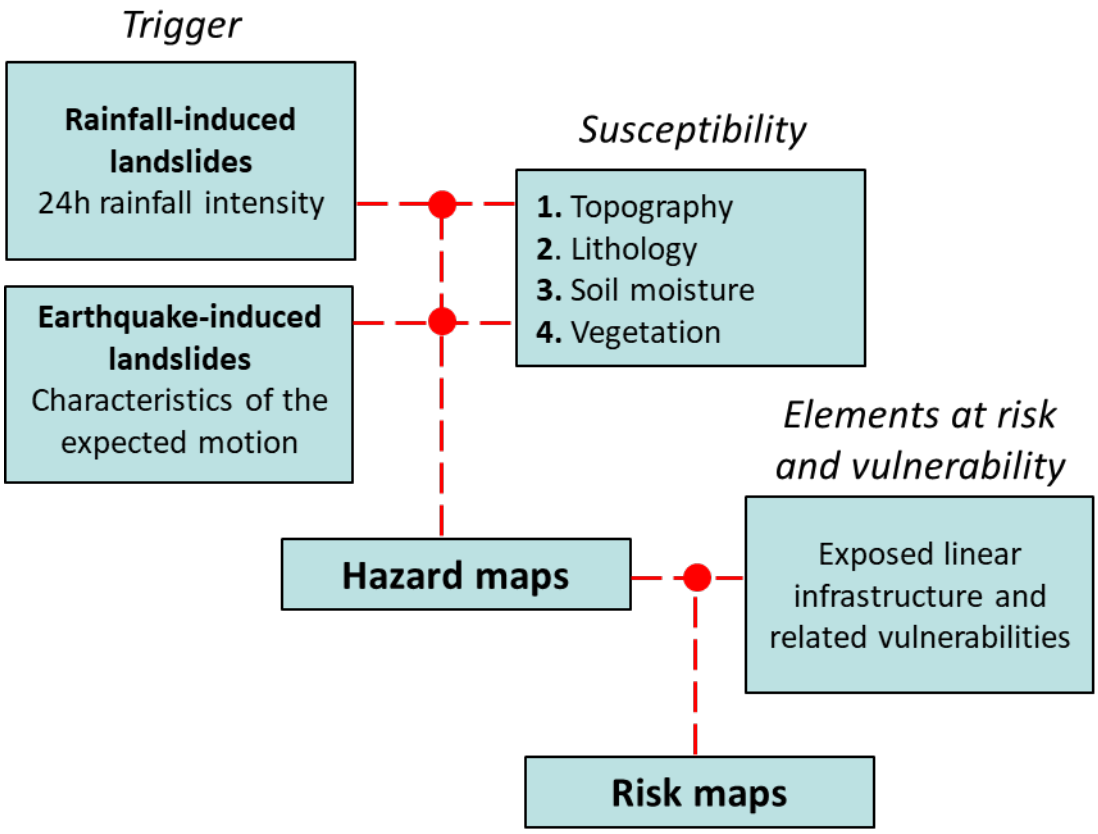

Figure 1 Flowchart of the landslide hazard model and risk assessment for critical infrastructure.

3. GIRI landslide susceptibility

In the GIRI landslide hazard model, the susceptibility map is used to distinguish landslide-prone areas. The susceptibility map has been derived by combining the information contained in global open-source datasets describing the topography (slope angle), lithology, vegetation and soil moisture information (Table 1). It classifies the globe into five landslide susceptibility categories corresponding to "Very Low", "Low", "Moderate", "High", and "Very High" susceptibility. Additionally, global landslide database for rainfall-induced landslides has been employed to visually analyse the outputs of the GIRI landslide susceptibility map for rainfall-induced landslides.

In the following subsections the input datasets that were uses for the computation of susceptibility and the method applied to obtain the susceptibility factors are introduced first. Then the method to compute the overall landslide susceptibility is explained in more detail.

Table 1 Datasets used in the GIRI landslide susceptibility model for rainfall-induced Landslides.

Type	Type of landslide	Source	Coverage	Resolution
Slope	Rainfall-induced Earthquake-induced	Derived from MERIT-Hydro DEM	Global	0,00083 ≈ 90 m
Lithology	Rainfall-induced	Global Lithological Map	Global	Polygon data

	Earthquake-induced	database (GLiM)		
Soil moisture	Rainfall-induced	Current climate: W5E5 Future climate: IPSL-CM6A-LR model from the ISIMIP3b data set SSP126 and SSP585 scenarios	Global	0.5°
	Earthquake-induced	ERA5 soil moisture climatology	Global	0.25°
Land cover	Rainfall-induced Earthquake-induced	ICDR Land Cover 2020	Global	0.002778°
Landslide database	Rainfall-induced	COLOR - NASA	Global	Point data

3.1. From input data to susceptibility factors

Slope factor

The slope calculation was done using the open-access software Whitebox Geospatial Analysis Tools (Whitebox GAT) developed by Lindsay (2016). The Slope tool uses the 3 × 3 polynomial fitting method for equal angle grids, as described by Florinsky (2016) and Florinsky (2017). The calculations are based on the spaceborne MERIT digital elevation model (DEM) by (Yamazaki et al. 2017), in a geographic coordinate system (WGS84). The pixels with DEM data are in angular units with a 3" resolution (~90 metres at the equator). The data are available as 5-degree × 5-degree tiles (6000 pixels × 6000 pixels), compressed into 30-degree × 30-degree packages.

Due to the large number of files (1150) and data size, the process was carried out in a series of (parallelised) Python scripts. These scripts are implemented by using Multiprocessing. It is an iterative procedure, that is tailored towards the data structure and the parallelization of the calculations, while the actual processing of each tile is implemented as a subclass.

To avoid edge contamination in the slope analysis, the DEM was first pre-processed (mosaicked) into a single global raster containing all files using the GDAL Virtual Format. From this dataset, GDAL Translate was used to extract a new set of buffered tiles, using 5 pixels as the buffer size. The buffer size is the number of pixels multiplied by the pixel size (3 arc seconds) measured in degrees.

The first step calculates the slope and stores the output in the same structure as the original DEM. The second step reads and transforms all layers (vegetation, lithology, moisture, and slope) into tiles with the same resolution as the original DEM. The third step loads all the layers from the previous and transforms layers into susceptibility factors and calculates susceptibility. The fourth step reclassifies

the susceptibility into susceptibility classes (1 to 5). The output is structured according to the same groups and tiles as the original DEM.

The slope data were then reclassified by an expert using information on landslide frequency distributions in the world. Cells were distributed in the six different susceptibility categories (0 – 5) according to their susceptibility degree as presented in Table 1. Intuitively the greater the slope angle the more susceptible the terrain is. However, since most soils have internal friction angles smaller than 36°, slopes steeper than 36° are not likely to be covered by sediments. The sediments on the slope have most likely already been removed in the past, and the slopes steeper than 50° might now consist primarily of hard rock. To account for this, the susceptibility factor for very steep slopes (greater than 36°) has been set to decrease. It is important to notice that for slopes which angle is less than 6° (i.e. for flat or nearly flat areas), the slope factor has been set equal to zero because the resulting landslide hazard is negligible even if all the other factors are favourable.

Table 2 Susceptibility index assigned to each slope class.

Range of slopes angle (unit: 1/100 degrees)	**Classification**	S_r
0000 – 0600	Very low	0
0601 – 1200	Low	1
1201 – 1800	Moderate	2
1801 – 2400	Medium	3
2401 – 3000	High	4
3001 – 3600	Very high	5
3601 – 4000	Probably stiff soil	4
4001 - 4400	Probably rock	3
4401 - 5000	Probably hard rock	2
> 5000	Stable hard rock	1
No Data	No Data	No Data

Lithology factor

Soil properties play a key role in determining slope stability. Ideally, detailed geotechnical information on the soil cover should be used to determine if the conditions for landslide initiation are met. However, at the global scale, only a general lithological description of the various locations is available. Therefore, assessing the terrain susceptibility using the information available about sediment strength at the global scale has been challenging.

In this study, we have utilized the information contained in the Global Lithological Map database (referred to as GLiM - Hartmann and Moosdorf, 2012). GLiM was constructed by compiling existing regional geological maps which were translated into lithological information using relevant regional literature. The database encompasses 1,235,400 polygons and employs a three-layer classification system for lithology. The first level contains 16 lithological classes that are comparable to previously applied definitions in global lithological maps. The two additional levels consist of 12 and 14 subclasses, respectively, offering more detailed descriptions of specific rock attributes.

For the purpose of our work, we have rasterized the GLiM to match the resolution of the slope map. The information of the lithology classes and subclasses were used to reclassify the world into three susceptibility classes (1 – 3) representing lithologies with low, moderate and high relevance for landslide susceptibility.

Soil moisture factor

Soil moisture plays a relevant role in slope stability. As water infiltrates into the soil, pore pressures increase and shear strength decreases eventually leading to failure if the soil strength is low and the slope is steep. In the GIRI landslide susceptibility assessment for rainfall-induced landslides, rainfall data with a spatial resolution of 0.5° has been used as a proxy to assess the soil moisture conditioning factors. This method has allowed to obtain susceptibility maps for different future climate scenarios.

For the period 1979-2016 the W5E5 precipitation estimates (Lange 2019) have been employed. More specifically the daily product that contains the sum of rainfall and snow water equivalent has been employed to obtain the mean value of the 38 rainfall maximum monthly cumulates.

For the periods 2061-2100 the IPSL-CM6A-LR model from the ISIMIP3b data set (Frieler et al. 2017) SSP126 and SSP585 scenarios have been employed to obtain the mean of the average monthly precipitation.

The distribution of the mean year maximum monthly rainfall in current climate conditions has been investigated (Figure 2a). Wetter areas are generally more susceptible to rainfall-induced landslides than drier areas. This criterion has been considered to classify the mean year maximum monthly rainfall into five classes (Table 3), and assign a soil moisture susceptibility factor (S_p).

145 *Table 3 Soil moisture susceptibility factor assigned for each of the mean year maximum monthly rainfall categories.*

Mean Year maximum monthly rainfall (MYMMR) (mm)	S_p
≤ 125	1
125 < MYMMR ≤ 250	2
250 < MYMMR ≤ 500	3
500 < MYMMR ≤ 1000	4
MYMMR > 1000	5

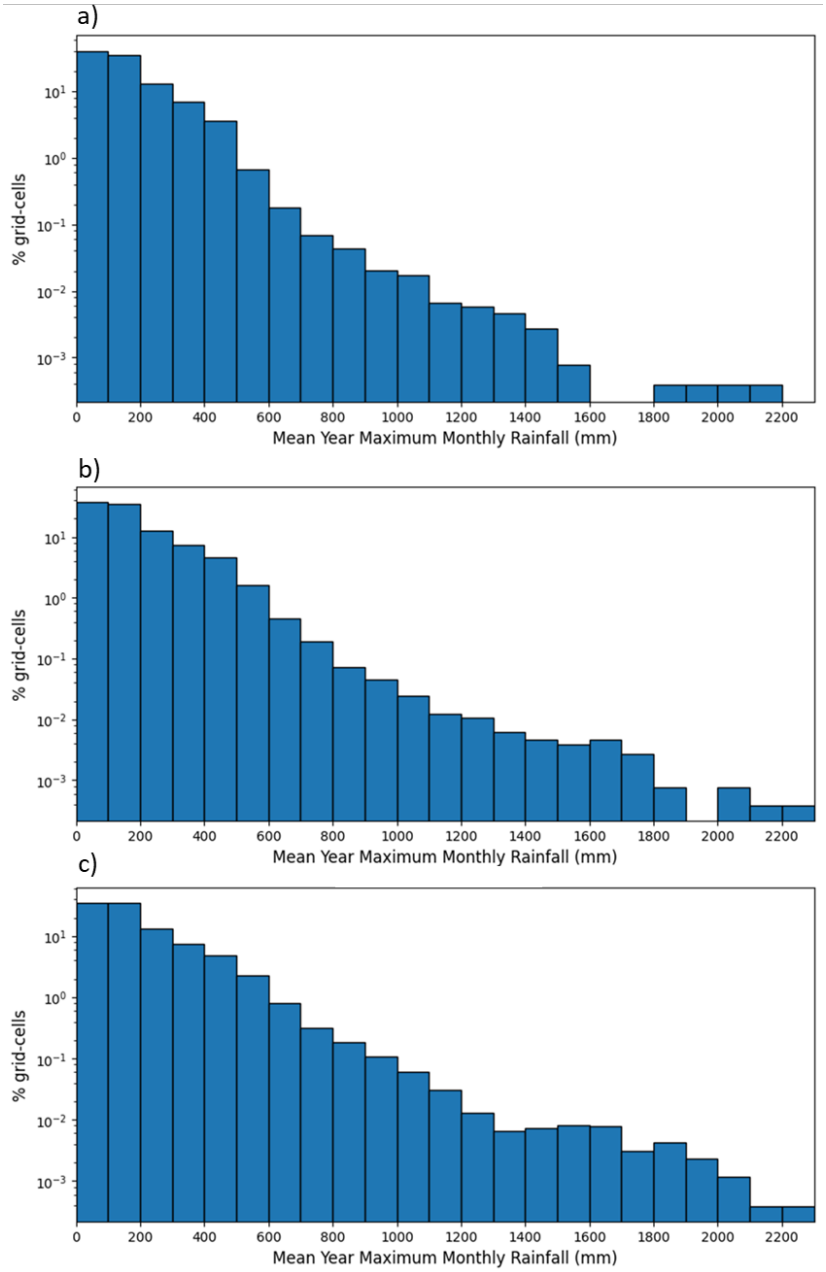

Figure 2 Mean year maximum monthly precipitation in (a) current climate conditions and in the period 2061-2100 with the (b) SSP126 and SSP585 climate change scenarios.

Figure 2 shows area affected by a given mean year monthly rainfall amounts for the current climate, and the two analysed future climate change scenarios (Figures 2b, and 2c). As it can be observed, it is expected that in future, the area affected by high mean year maximum monthly rainfall amounts is going to slightly increase. This observation might seem counterintuitive but can be explained by changes in the spatial distribution of the rainfall.

In the future, some regions will experience higher rainfall accumulations compared to present conditions, while other areas might receive less rainfall. As a result, the overall effect is a modest increase in the mean year maximum monthly rainfall across a larger geographic area.

For the case of earthquake-induced landslides, the soil moisture information in the Essential Climate Variables for assessment of climate variability from 1979 to present dataset (Hersbach et al. 2018) was employed. This dataset is based on the provisional data from ECMWF's ERA5 data. Soil moisture information consists of the monthly volumetric water content climatology obtained from satellite observations in the top 7 cm of soil with a spatial resolution of 0.25°. For this work, the mean soil moisture in each of the pixels has been used.

Table 4 Soil moisture susceptibility factor assigned for each of the volumetric water content categories.

Volumetric water content (VWC) (m^3/m^3)	S_p
≤ 0.16	1
$0.16 < VWC \leq 0.36$	2
$0.36 < VWC \leq 1$	3

Vegetation factor

Vegetation can play a significant role in slope stability by providing additional cohesion to the soil and reducing soil moisture by means of evapotranspiration. Additionally, being able to distinguish between areas with vegetation cover and unvegetated areas can provide an indication of the soil availability. The C3S Land Cover v2.1 global ICDR Land Cover map for 2000 has been used (Copernicus Climate Change Service, Climate Data Store 2019; Defourny et al. 2021) in this study. The land cover map has a regular latitude-longitude grid with a 0.002778° resolution (approximately 300 m at the equator). Each pixel indicates a categorical land cover class defined using UN Land Cover Classification System classifiers.

Here the original 38 categories from the land cover map have been re-classified using expert criteria and information contained in relevant literature into five classes with relation to non-resistance to landslides.

Table 5 Susceptibility factor for the land cover classes.

Land cover class	S_v
Bare areas	5
Sparse vegetation	4
Grassland	5
Evergreen shrubs	4
Shrubs	3
Close Forest	2
Open Forest	3
Agriculture	5
Agriculture with herbaceous cover	4
Agriculture combined with shrubs and forest	3
Water bodies	0
Permanent Ice	1
Urban areas	1

3.2. Method

The method to obtain landslide susceptibility is similar to that of Nadim et al. (2006), Nadim et al. (2013), and Jaedicke et al. (2014). Landslide susceptibility is computed as follows:

$$S = \prod_i w_i \cdot f(S_i) \qquad (1)$$

Where S_i are the slope, lithology, vegetation and mean of the annual monthly rainfall factors, and w_i are the weights of the slope, lithology, vegetation and mean of the annual monthly rainfall factors respectively. The weights of different susceptibility factors were calibrated to the information available in landslide inventories and physical processes.

4. Assessment of the landslide triggering conditions

4.1. Rainfall triggering conditions

Shallow slides and debris flows are generally triggered by severe short-duration high-intensity rainfall events. Rainfall intensity-duration (I-D) thresholds are commonly used in regional-scale landslide early warning systems to assess the hazard represented by a given rainfall situation. To determine the magnitude of a rainfall situation the GIRI model uses 24 h rainfall data to assess the return period of a given rainfall event.

To determine the rainfall triggering potential the 24 h rainfall product from the W5E5 dataset (Lange 2019) has been employed to normalize the 24 h rainfall intensity of a given rainfall scenario as follows:

$$I_{24h-norm} = \frac{I_{24h} - \mu_{I_{max}}}{\sigma_{I_{max}}} \quad (2)$$

Where I_{24h} represents the rainfall event 24 h rainfall intensity, $\mu_{I_{max}}$ is the mean value of maximum annual 24-hr rainfall intensity at location of interest, and $\sigma_{I_{max}}$ represents the standard deviation of maximum annual 24-hr rainfall intensity at location of interest.

The 24h duration 5 years, 25 years, 200 years, and 1000 years return periods have been selected as thresholds to distinguish between five rainfall hazard classes. Table 5 shows the correspondence between $I_{24h-norm}$ and rainfall return period Assuming a Gumbel distribution for the maximum annual daily rainfall at a given location.

Table 6 Correspondence between $I_{24h-norm}$ and return pe obtained of rainfall 24h intensity.

$I_{24hr\text{-}normalised}$	**Return period (years)**
0.70	4.9
0.72	5
1.13	10
1.86	20
2.0	23.7
2.6	50
3.1	100
3.7	200
4.4	500
4.9	1000
5.0	1087

It will take a long time (centuries) for the terrain to adapt to a new climate regime. Therefore, for future climate scenarios, the normalisation of the triggering rainfall should be done with respect the values of $\mu_{I_{max}}$ and $\sigma_{I_{max}}$ obtained for today's climate. This approach will capture the change in the characteristics of the triggering rainfall in the future.

4.2. Earthquake triggering conditions

The model for earthquake-triggered landslide hazard developed for the GAR reports (Nadim et al. 2013) used the peak ground acceleration (PGA) from the Global Seismic Hazard Program, GSHAP

(Giardini et al. 2000; Giardini et al. 2003). The 475-year return period (10% probability of exceedance in 50 years) was employed in that model to determine the earthquake triggering potential. Based on the calibrations done previously for the GAR model, for the GIRI model, PGA values of 0.05g, 0,15g, 0.25g, 0.35g and 0.45g were selected as thresholds to define five seismic hazard classes. We have considered that earthquakes with a PGA smaller than 0.05g have a negligible probability of triggering a landslide.

5. Scenario-based landslide hazard on roads and railways

The "landslide hazard index", i.e., the probability of landslide occurrence for a specific triggering event, is derived from the combination of susceptibility index and the rainfall triggering conditions, or the susceptibility index and the earthquake triggering conditions. The combination of the susceptibility and the rainfall triggering conditions is done according to the hazard matrix in Figure 3.

$I_{24hr\text{-}normalised}$	Susceptibility category				
	Susc. 1	Susc. 2	Susc. 3	Susc. 4	Susc. 5
$I_{24hr\text{-}normalised} < 0.3$	~ 0	~ 0	~ 0	~ 0	~ 0
$0.3 \leq I_{24hr\text{-}normalised} < 2.0$	~ 0	~ 1	2%	3%	5%
$2.0 \leq I_{24hr\text{-}normalised} < 3.7$	~ 0	2%	3%	5%	10%
$3.7 \leq I_{24hr\text{-}normalised} < 5.0$	~ 0	3%	5%	10%	15%
$I_{24hr\text{-}normalised} \geq 5.0$	~ 0	5%	10%	15%	20%

Figure 3 Hazard matrix used to determine the probability of occurrence of a significant rainfall-induced landslide that impacts the 1km stretch of the road or railway as function of $I_{24h-norm}$ of the precipitation scenario at that location and the Susceptibility Category.

The global (rainfall-triggered) landslide hazard index map has been integrated over rainfall events with different return periods to “translate” the combination of landslide hazard category and return period of the daily rainfall into the probability of landslide occurrence within an area.

The probabilities of each assigned to each hazard class have been calibrated such that the integration over all the return periods for the whole globe results in an annual number of significant rainfall-induced landslides (~400,000 globally) that is consistent with the data presented in the Global Landslide Hazard Map (The World Bank 2020).

Similarly, for the case of earthquake-induced landslides, the combination of the susceptibility and the earthquake triggering conditions is done according to the hazard matrix in Figure 4. If PGA is less than 0.05g, then the probability of triggering an earthquake-induced landslide is negligible even for

high susceptibility categories. The probabilities of each hazard class have been calibrated such that the total number of significant landslides triggered by earthquakes is consistent with the approximate 130,000 landslides happening globally each year, as indicated by the World Bank report (The World Bank 2020).

PGA (g)	Susceptibility category				
	Susc. 1	Susc. 2	Susc. 3	Susc. 4	Susc. 5
0.05g ≤ PGA < 0.15g	~ 0	~ 0	~ 0	0.1%	0.5%
0.15g ≤ PGA < 0.25g	~ 0	~ 0	0.1%	0.5%	1%
0.25g ≤ PGA < 0.35g	~ 0	0.1%	0.5%	1%	5%
0.35g ≤ PGA < 0.45g	~ 0	0.5%	1%	5%	10%
PGA ≥ 0.45g	~ 0	1%	5%	10%	40%

Figure 4 Probability of occurrence of a significant earthquake-induced landslide that impacts the 1km stretch of the road or railway in question as function of PGA of the earthquake scenario at that location and the Susceptibility Category.

To assess hazard possessed by landslides on linear infrastructure we have used a unit of 1km length along the road or railway and a 300 m buffer on each side of the road or railway stretch (Figure 5). The pixel with highest susceptibility for earthquake-induced landslide in the 1km × 600m unit has been used to determine the probability of a landslide impacting the 1 km stretch of the road or railway in question (indicated in Figure 3 and Figure 4).

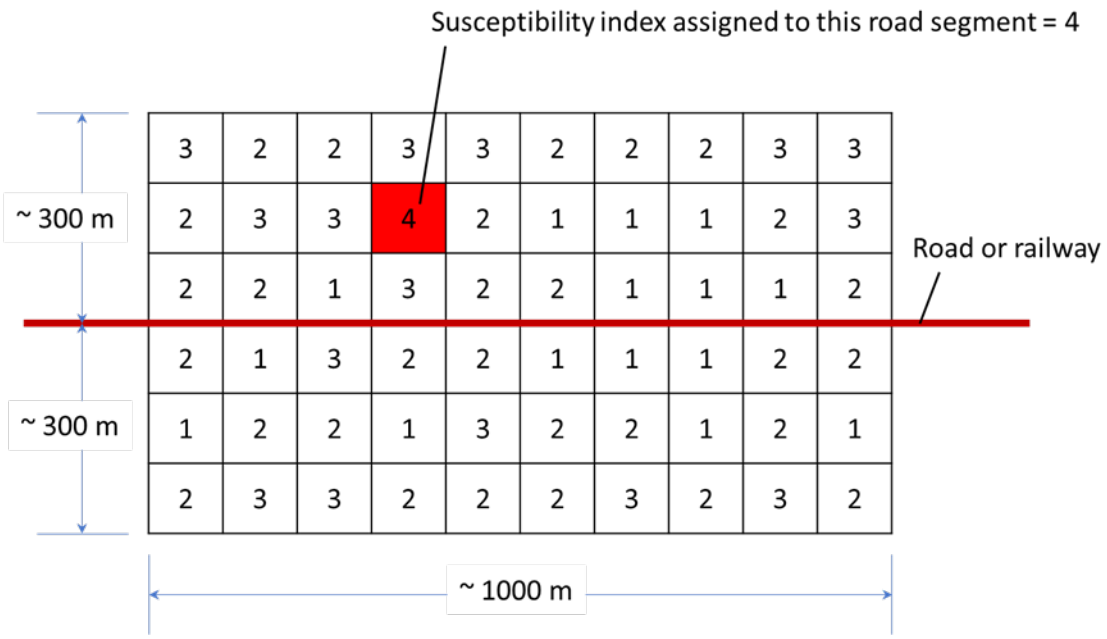

Figure 5 Schematic of buffer zones around a 1km stretch of road or railway, and assigning the susceptibility index. Each box in the figure represents a pixel and the number shown in the box represents the landslide susceptibility class.

6. Results

Figure 6 shows the susceptibility map for rainfall-induced landslides obtained with the GIRI model for current climate conditions. As expected, the areas exhibiting a higher susceptibility to landslides coincide rather well with mountainous areas that have a relatively humid climate. This fact can be explained because the slope factor plays a relevant role in susceptibility assessment.

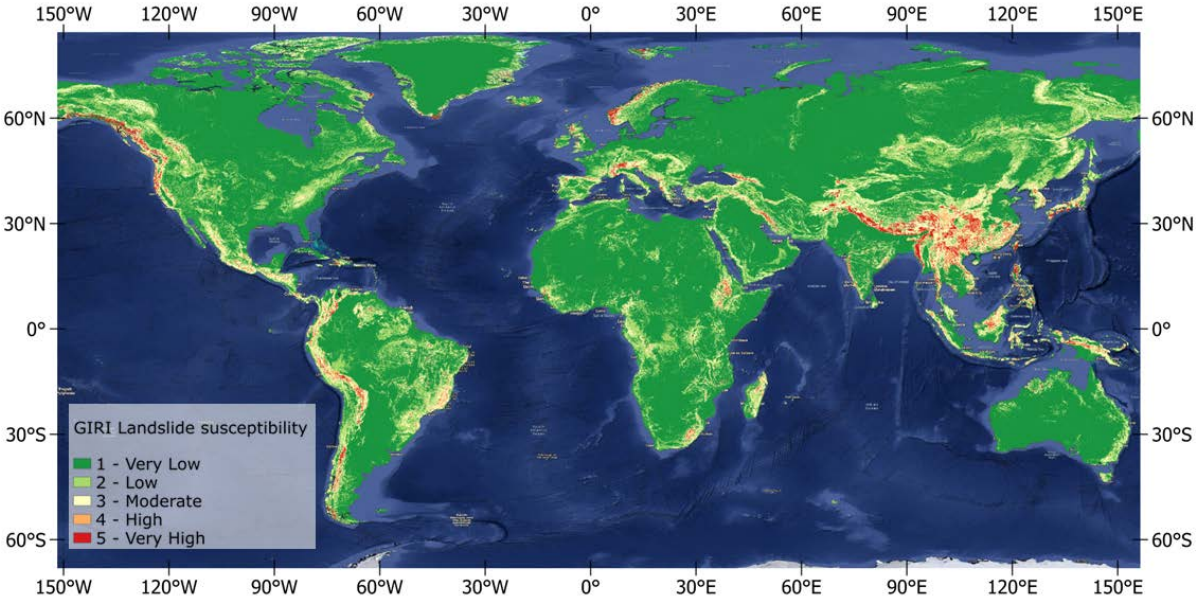

Figure 6 Susceptibility to rainfall-induced landslides obtained with the GIRI model for current climate conditions.

Evaluating the performance of landslide susceptibility maps at a global scale is challenging because of the limitations of global landslides databases. Here, the rainfall-induced landslides in the global NASA COLOR database (Juang et al. 2019), and from selected national (Ekker et al. 2013) and regional (Palau et al. 2022) inventories have been used for the visual inspection of our results for current climatic conditions. Generally, the location of the landslides in the coincide rather well with high susceptibility areas. Figure 7 shows a zoom over south-east Asia. It can be observed that the areas with higher susceptibility coincide with the Himalayas, the Western Ghats, and the Zagros mountainous areas where most landslides have been reported.

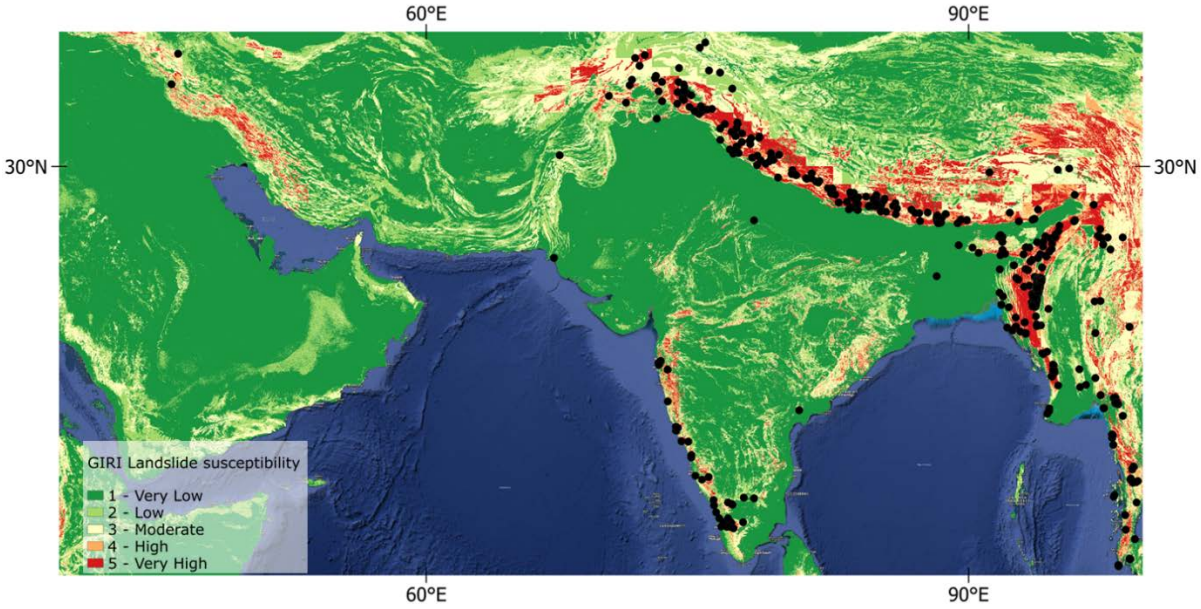

Figure 7 Susceptibility to rainfall-induced landslides obtained with the GIRI model for current climate conditions over the South-East of Asia. The Black points represent the Landslides in the NASA COLOR database (Kirschbaum et al. 2010; Juang et al. 2019).

Landslide susceptibility maps for the present and the two analysed future climate change scenarios (Figures 8a and 8b) are generally similar. However, some areas, such as the northwest of America and the southeast of Asia, exhibit a slight increase in susceptibility. This increase is larger for the SSP585 scenario than for the SSP126 scenario (Figures 8a and 8b). On the other hand, our model predicts that landslide susceptibility will decrease slightly in some other areas, like Central America and the Iberian Peninsula. However, one must remember that this change in susceptibility is only due to the change in the average long-term precipitation regime. It could be the case that landslide hazard changes more dramatically if the frequency of high-intensity rainfall events decreases or increases.

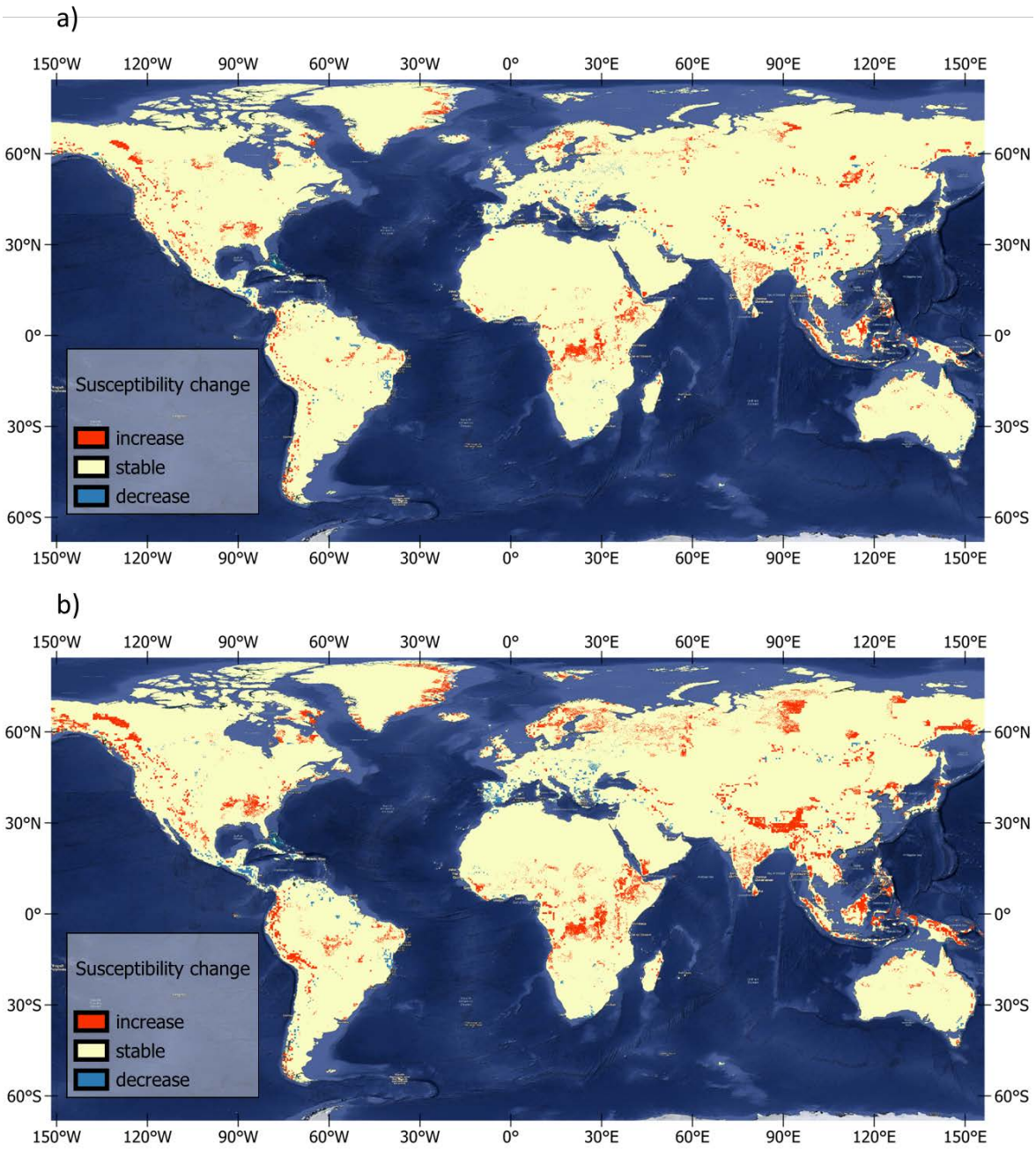

285 *Figure 8 (a) Difference between the susceptibility map for rainfall-induced landslides with today's climate and the susceptibility map for the future climate assuming an SSP126 scenario. (b) Difference between the susceptibility map for today's climate and future climate assuming an SSP585 scenario.*

Similarly, for the case of earthquake-induced landslides the areas that exhibit a high susceptibility generally coincide with the locations of mountainous areas. When compared to the susceptibility map
290 for current climate conditions, it can be noticed that the earthquake-induced landslides susceptibility map displays a higher susceptibility in the south-east Asia and western America, and a lower susceptibility in western Norway. This can be explained because the soil moisture factor has a smaller weight in the model for earthquake-induced landslides. Thus, slope angle is more relevant in determining earthquake-induced landslide susceptibility.

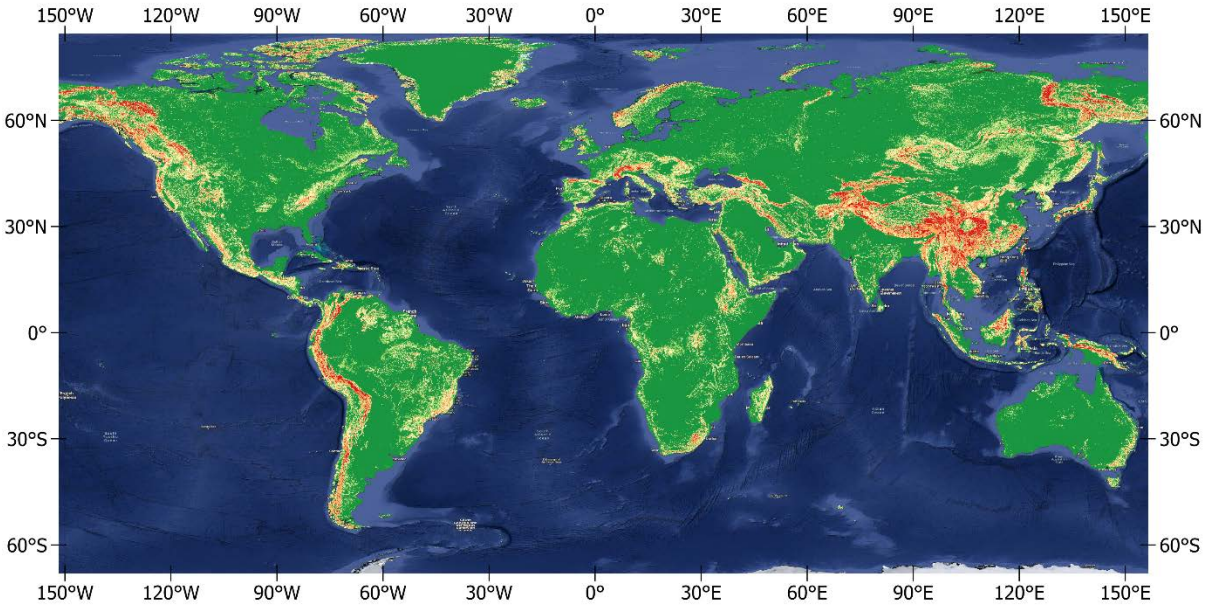

Figure 9 Susceptibility to earthquake-induced landslides obtained with the GIRI model.

7. Discussion and conclusions

A new model to probabilistically assess landslide hazard at a global scale has been developed. The GIRI landslide hazard model is used in the Flagship Report of The Coalition for Disaster Resilient Infrastructure (CDRI) to evaluate the global risk posed by landslides to road and railway infrastructure, both for the present climate regime and for future climate scenarios.

The GIRI landslide hazard model uses information on the terrain slope angle, lithology, soil moisture and vegetation to obtain a susceptibility map. Then the susceptibility map can be combined with information on the rainfall or earthquake landslide triggering conditions to obtain a fully probabilistic hazard map or used in a scenario-based approach with Monte Carlo simulations to assess the risk to critical infrastructure (or to other elements at risk).

The resolution of the GIRI landslide model is much higher than the resolution of the previous similar global models. This is mainly because more up-to-date datasets to describe the lithology, vegetation, soil moisture and the terrain slope angle have been employed. In past studies (Nadim et al. 2006; Nadim et al. 2013; Jaedicke et al. 2014) a DEM with a resolution of 30 arc second was used. Here we have applied a DEM with a resolution of 3 arc seconds, which corresponds to approximately 90m at the equator. This has allowed a better representation the slope angle over the world.

Another significant difference with previous models is that for the case of rainfall-induced landslides, the mean of the year maximum monthly precipitation has been used as a proxy to account for soil

moisture preconditioning. This has allowed obtaining susceptibility maps for the current climate conditions, as well as for the future SSP126 and SSP585 climate change scenarios.

The evaluation of the performance of landslide susceptibility maps has been challenging because of the limitations in global landslide inventories, which are rather incomplete. Generally, the areas that exhibit a higher susceptibility coincide rather well with mountainous areas where landslides have been reported in global and national landslide databases (Ekker et al. 2013; Juang et al. 2019; Palau et al. 2022).

The comparison of the susceptibility maps for rainfall-induced landslides obtained for the current climate conditions, and the susceptibility maps obtained for the SSP126 and SSP585 scenarios shows a slight increase of susceptibility in some areas that will be affected by larger rainfall amounts. Susceptibility will decrease slightly in other areas, like Central America and the Iberian Peninsula. The areas where susceptibility will change in future are larger for the SSP585 climate change scenario Than for the SSP126 scenario. It should be pointed out that the change in landslide susceptibility predicted by the GIRI is only due to modification in the prevailing long-term precipitation patterns. Land use changes can also affect susceptibility, and landslide hazard could undergo even more pronounced changes if the frequency of occurrence of intense rainfall events rises or falls in the future.

In this study, the hazard due to rainfall-induced and earthquake-induced landslides were analysed separately. This decision was taken mainly because the susceptibility factors for the two triggering mechanisms might be different. Additionally, the risk (to human life) due to earthquake-induced landslides is often included in the earthquake risk, and one should avoid counting the same risk twice in a multi-hazard and multi-risk context.

The rainfall triggering conditions are based on an extreme-value analysis of 1-day precipitation, as opposed to the extreme monthly precipitation used in the GAR model (Nadim et al. 2006; Nadim et al. 2013). The earthquake triggering conditions are assessed in a scenario-based approach using the PGA of a simulated earthquake event at a given location.

An important limitation of the GIRI landslide model is that it does not account for human-induced landslides. Such landslides generally have high economic consequences, such as road and railway closures, but rarely result in fatalities. Accounting for the human factor is not straightforward, as it depends on human decisions that are not easy to predict. In future, a population density factor could be introduced to account for the increased chance of having a landslide triggered by human activity in densely populated areas.

The developed GIRI landslide hazard model enables the user to obtain an event-based landslide hazard over road and railways. The employed methodology in the GIRI model by combining susceptibility information and information on the triggering factors is very similar to the approach

used in regional-scale and global-scale landslide early warning systems (Kirschbaum et al. 2009; Krøgli et al. 2018; Palau et al. 2020). However, most of the regional and global-scale landslide early warning systems usually adopt a qualitative or fuzzy logic approach. The GIRI landslide model output is fully probabilistic hazard along linear infrastructures. This is relevant for risk assessment.

The susceptibility maps and hazard outputs provided by the GIRI model should only be utilized to gain a general understanding of landslide susceptibility and hazard distribution in current and future climate conditions. Due to the limitations of the input parameters and the calibration of our model, the presented results cannot be applied to assess the landslide hazard at a regional scale, nor for urban planning.

It is not straightforward to evaluate the vulnerability of road, railway and other components of a transportation infrastructure in our model. The intensity measure used for characterising landslides in physical vulnerability models is depth and/or velocity of sediments upon impact, neither of which are estimated in our model. Further work needs to be done in order to be able to quantify landslide magnitude at the scale of the analysis.

Acknowledgements and Funding

This work has been funded by the Coalition for Disaster Resilient Infrastructure (CDRI) Global Infrastructure Risk Index (GIRI) project. We acknowledge ESA CCI Land Cover and the EC C3S Land cover project for providing global-scale land cover information.

References

Caine N (1980) The rainfall intensity-duration control of shallow landslides and debris flows. Geografiska Annaler 62A:23–27

Copernicus Climate Change Service, Climate Data Store (2019) Land cover classification gridded maps from 1992 to present derived from satellite observation. Copernicus Climate Change Service (C3S) Climate Data Store (CDS). https://doi.org/10.24381/cds.006f2c9a

Defourny P, Lamarche C, Marissiaux Q, Brockmann C, Martin B, Kirches G (2021) Product User Guide and Specification: ICDR Land Cover 2016-2020

Dilley M (2005) Natural disaster hotspots: a global risk analysis. World Bank, Washington, D.C

Ekker R, Kværne K, Os A, Humstad T (2013) regObs - public database for submitting and sharing observations. In: International Snow Science Workshop. Grenoble, Chamonix Mont-Blanc, p 5pp

Florinsky I (2016) Digital Terrain Analysis in Soil Science and Geology - 2nd Edition, 2nd edn. Academic Press

Florinsky IV (2017) Spheroidal equal angular DEMs: The specificity of morphometric treatment. Transactions in GIS 21:1115–1129. https://doi.org/10.1111/tgis.12269

Frieler K, Lange S, Piontek F, Reyer CPO, Schewe J, Warszawski L, Zhao F, Chini L, Denvil S, Emanuel K, Geiger T, Halladay K, Hurtt G, Mengel M, Murakami D, Ostberg S, Popp A, Riva R, Stevanovic M, Suzuki T, Volkholz J, Burke E, Ciais P, Ebi K, Eddy TD, Elliott J, Galbraith E, Gosling SN, Hattermann F, Hickler T, Hinkel J, Hof C, Huber V, Jägermeyr J, Krysanova V, Marcé R, Müller Schmied H, Mouratiadou I, Pierson D, Tittensor DP, Vautard R, van Vliet M, Biber MF, Betts RA, Bodirsky BL, Deryng D, Frolking S, Jones CD, Lotze HK, Lotze-Campen H, Sahajpal R, Thonicke K, Tian H, Yamagata Y (2017) Assessing the impacts of 1.5°C global warming – simulation protocol of the Inter-Sectoral Impact Model Intercomparison Project (ISIMIP2b). Geoscientific Model Development 10:4321–4345. https://doi.org/10.5194/gmd-10-4321-2017

Froude MJ, Petley DN (2018) Global fatal landslide occurrence from 2004 to 2016. Natural Hazards and Earth System Sciences 18:2161–2181. https://doi.org/10.5194/nhess-18-2161-2018

Gariano SL, Guzzetti F (2016) Landslides in a changing climate. Earth-Science Reviews 162:227–252. https://doi.org/10.1016/j.earscirev.2016.08.011

Giardini D, Grünthal G, Shedlock K, Zhang P (2000) 74 the GSHAP global seismic hazard map. Seismological Research Letters 42. https://doi.org/10.1785/gssrl.71.6.679

Giardini D, Grünthal G, Shedlock KM, Zhang P (2003) The GSHAP Global Seismic Hazard Map. In: International Handbook of Earthquake and Engineering Seismology. Academic Press, pp 1233–1239

Guzzetti F, Peruccacci S, Rossi M, Stark CP (2008) The rainfall intensity–duration control of shallow landslides and debris flows: an update. Landslides 5:3–17. https://doi.org/10.1007/s10346-007-0112-1

Hartmann J, Moosdorf N (2012) The new global lithological map database GLiM: A representation of rock properties at the Earth surface. Geochemistry, Geophysics, Geosystems 13. https://doi.org/10.1029/2012GC004370

Jaedicke C, Van Den Eeckhaut M, Nadim F, Hervás J, Kalsnes B, Vangelsten BV, Smith JT, Tofani V, Ciurean R, Winter MG, Sverdrup-Thygeson K, Syre E, Smebye H (2014) Identification of landslide hazard and risk “hotspots” in Europe. Bulletin of Engineering Geology and the Environment 73. https://doi.org/10.1007/s10064-013-0541-0

Juang CS, Stanley TA, Kirschbaum DB (2019) Using citizen science to expand the global map of landslides: Introducing the Cooperative Open Online Landslide Repository (COOLR). PLOS ONE 14:e0218657. https://doi.org/10.1371/journal.pone.0218657

Keefer, DK (1984) Landslides caused by earthquakes. Bull. Geol. Soc. Am. 95, 406–421.

Kirschbaum DB, Adler R, Hong Y, Hill S, Lerner-Lam A (2010) A global landslide catalog for hazard applications: method, results, and limitations. Natural Hazards 52:561–575. https://doi.org/10.1007/s11069-009-9401-4

Kirschbaum DB, Adler R, Hong Y, Lerner-Lam A (2009) Evaluation of a preliminary satellite-based landslide hazard algorithm using global landslide inventories. Natural Hazards and Earth System Sciences 9:673–686. https://doi.org/10.5194/nhess-9-673-2009

Krøgli IK, Devoli G, Colleuille H, Boje S, Sund M, Engen IK (2018) The Norwegian forecasting and warning service for rainfall- and snowmelt-induced landslides. Natural Hazards and Earth System Sciences 18:1427–1450. https://doi.org/10.5194/nhess-18-1427-2018

Lange S (2019) WFDE5 over land merged with ERA5 over the ocean (W5E5)

Lindsay JB (2016) Whitebox GAT: A case study in geomorphometric analysis. Computers & Geosciences 95:75–84. https://doi.org/10.1016/J.CAGEO.2016.07.003

Nadim F, Jaedicke C, Smebye H, Kalsnes B (2013) Assessment of Global Landslide Hazard Hotspots. In: Sassa K, Rouhban B, Briceño S, McSaveney M, He B (eds) Landslides: Global Risk Preparedness. Springer, Berlin, Heidelberg, pp 59–71

Nadim F, Kjekstad O, Peduzzi P, Herold C, Jaedicke C, Kjekkstad O (2006) Global landslide and avalanche hotspots. Landslides 3:159–173. https://doi.org/10.1007/s10346-006-0036-1

Palau RM, Berenguer M, Hürlimann M, Sempere-Torres D (2022) Application of a fuzzy verification framework for the evaluation of a regional-scale landslide early warning system during the January 2020 Gloria storm in Catalonia (NE Spain). Landslides. https://doi.org/10.1007/s10346-022-01854-2

Palau RM, Hürlimann M, Berenguer M, Sempere-Torres D (2020) Influence of the mapping unit for regional landslide early warning systems: comparison between pixels and polygons in Catalonia (NE Spain). Landslides 17:2067–2083. https://doi.org/10.1007/s10346-020-01425-3

Petley D (2012) Global patterns of loss of life from landslides. Geology 40:927–930. https://doi.org/10.1130/G33217.1

The World Bank (2020) The Global Landslide Hazard Map. London, United Kingdom

Yamazaki D, Ikeshima D, Tawatari R, Yamaguchi T, O'Loughlin F, Neal JC, Sampson CC, Kanae S, Bates PD (2017) A high-accuracy map of global terrain elevations. Geophysical Research Letters 44:5844–5853. https://doi.org/10.1002/2017GL072874

Zhang, S, Zhang LM, Glade T (2014) Characteristics of earthquake- and rain-induced landslides near the epicenter ofWenchuan earthquake. Engineering Geology 175 (2014) 58-73